RESEARCH ARTICLE

Droplets and jet in solvents

Formation of microfluidic droplets and jets in a solvent-rich oil phase

Victoria Joseph and Thomas Cubaud*

Department of Mechanical Engineering, Stony Brook University, NY 11794 USA
*Corresponding author: thomas.cubaud@stonybrook.edu

Received:----; Revised:----; Accepted:-----;

Keywords: Spontaneous emulsification; Solvent shifting; Isopropanol; Wetting; Miscible

Abstract

We develop original flow-based methods to interrogate and manipulate out-of-equilibrium behaviour of ternary fluids systems at the small scale. In particular, we examine droplet and jet formation of ternary fluid systems in coaxial microchannels when an aqueous phase is injected into a solvent-rich oil phase using common fluids, such as ethanol for the aqueous phase, silicone oil for the oil phase, and isopropanol for the solvent. Alcohols are often employed to impart oil and water properties with a myriad of practical uses as extractants, antiseptics, wetting agents, emulsifiers or biofuels. Here, we systematically examine the role of alcohol solvents on the hydrodynamic stability of aqueous-oil multiphase flows in square microchannels. Broad variations of flow rates and solvent concentration reveal a variety of intriguing droplet and jet flow regimes in the presence of spontaneous emulsification phenomena and significant mass-transfer across the fluid interface. Typical flow patterns include dripping and jetting droplets, phase inversion and dynamic wetting, and conjugate jets. Functional relationships are developed to model the evolution of multiphase flows characteristics with solvent concentration. This work provides insights into complex natural phenomena relevant to the application of microfluidic droplet systems to chemical assays as well as fluid measurement and characterization technologies.

Impact Statement

The control of the phase behaviour of ternary fluid systems represents a considerable technological challenge with the formation of complex flow and transport phenomena at the fluid interface. Systems composed of two immiscible fluids, such as water and oil, and a miscible solvent, however, are commonly employed during the formation of microemulsions and find use in a variety of industries, including in the pharmaceutical and energy sectors and in consumer products, such as food and cosmetics. While numerous studies have addressed the thermodynamic stability of ternary systems at long time-scales, less is known about their out-of-equilibrium behaviour at short timescales, which limits the development of advanced functional materials. In this work, we reveal powerful flow-based microfluidic techniques for the formation of aqueous droplets and jets in solvent-oil mixtures and lay the phenomenological and mathematical foundations for the manipulation of ternary fluid systems and time-evolving soft materials in microflow reactors.

1. Introduction

Liquid multiphase flow processing techniques are commonly encountered in a wide range of industries, including in the energy and pharmaceutical domains as well as food, cosmetics, 3-D printing, and material synthesis (Aubry, et al. 2009; Zinchenko & Davis 2017; Rauzan, et al. 2018). As a condensed phase of matter, the liquid state is made of closely packed molecules and the property of fluidity confers unique

abilities for the transport and manipulation of basic materials, including water, oils, and organic solvents. Emulsions and interfacial fluid arrangements can be controlled using a variety of tensioactive agents (Leal-Calderon, Schmitt & Bibette 2007; Perazzo, Preziosi & Guido 2015). For instance, amphiphilic surfactant molecules are often added to water and oil dispersions during the formation of emulsions to reduce interfacial tension and stabilize droplets against coalescence (McClements 2012; Gupta, et al. 2016; Kim & Mason 2017). Recently, solutes of different types have been shown to facilitate the fabrication of all-aqueous biocompatible materials (Song, Sauret & Shum 2013). In general, however, the strong intermolecular forces present in these systems due to particulate additives introduce great complexity in the prediction of fluid interactions and flow patterns.

In the case of pure substances, the interfacial behaviour of immiscible fluids depends on the interplay of interfacial and viscous stresses (de Gennes, Brochard-Wyart & Quéré 2004), and capillary instabilities typically lead to the formation of dispersed flows of droplets (Eggers & Villermaux 2008; Montanero & Gañán-Calvo 2020). By contrast, when fluids are miscible, the interface is diffuse and separated flows, such as core-annular and layered flows, readily form depending on fluid viscosities and flow velocity (Selvam, et al. 2007; Hu & Cubaud 2018; Salin & Talon 2019). Diverse advection-diffusion phenomena are also observed between miscible fluids during displacement and transport in porous-like media (Lajeunesse, et al. 1999; Vanaparthy & Meiburg 2008; Soori & Ward 2018). While hydrodynamics and interfacial properties of pure fluids are usually well understood, much less is known about the flow behaviour of mixtures made of disparate liquids. In particular, for ternary fluid systems, the presence of a solvent that is miscible in both oil and water dramatically modifies local values of interfacial tension and viscosity, and introduces complex gradients of chemical potentials between phases depending on preparation and injection scheme (Dinh, Casal & Cubaud 2025). At equilibrium, the phase behaviour of ternary fluid blends is typically determined using titration experiments and Gibbs composition triangles delineate the various states of the mixture, including of regions of spontaneous emulsification, where fine dispersions naturally form (Vitale & Katz 2003; Solans, Morales & Homs 2016; Tan, et al. 2019). At short timescales, however, ternary fluid interactions in microchannels are dominated by sharp interfaces between fluids and complex solutal fluxes and Marangoni flows develop between droplets and conjugate phases. The use of miscible solvents with immiscible fluids find use in numerous extraction and purification processes (Mary, Studer & Tabeling 2008; Santana, et al. 2020; Chen, Deng & Luo 2023) and mass exchange between two liquid phases is driven by unbalanced chemical potentials. Complex fluid dynamic processes are observed at various time scales, such as solvent shifting (Haase & Brujic 2014; Hajian & Hardt 2015; Li, et al. 2021), which is not fully unraveled to date and difficult to control. Overall, These limitations hinder the development of future flow technology for the advanced treatment of oils and aqueous products with solvent additives.

Microfluidic technology provides unprecedented means to examine fluid interactions and out-of-equilibrium processes at short timescales with the precise control fluid streams in microgeometries (Squires & Quake 2005; Nunes, Constantin & Stone 2013; Xia, et al. 2021; Dinh, et al. 2024). In particular, regular arrays of monodisperse droplets can be finely tuned with flow rates of injection using a variety of fluid contactors, including T-junctions, focusing sections, and centreline injections (Baroud, Gallaire & Dangla 2010; Anna 2016; Doufène, et al. 2019; Nan, et al. 2024). Coaxial microchannels are practical for producing periodic multiphase flows patterns through centreline injection of the dispersed phase in the absence of significant wetting phenomena of small droplets (Utada, et al. 2007; Dinh & Cubaud 2021). While the field of microfluidic droplets find use in range of applications for encapsulation, mixing, and separation of components at the small scale, the stability of segmented flows of droplets in the presence of miscible solvent, however, is poorly understood to date. In particular, solvent concentration gradients drive considerable mass transfer across the interface and fluid recombination processes locally alter interfacial tension and droplet dynamics. It is, therefore, important to clarify the role of miscible fluid additives on microfluidic multiphase flows to better control solvent shifting and spontaneous emulsification phenomena at the small scale. Hence, new predictive knowledge is needed on the stability of microfluidic droplets in a solvent-rich phase to improve technical capabilities of microfluidic systems in the areas of fluid extraction and purification processes, and synthesis of time-evolving soft materials.

Here, we investigate the role of solvent concentration on microfluidic two-phase flows using coaxial microchannels. A solvent that is miscible in both the aqueous and the oil phases is preliminarily mixed with the oil before microfluidic injections. We examine in particular the situation where a low-viscosity aqueous phase is introduced in a solvent rich oil phase over a wide range of flow rates and

solvent concentrations. Three main flow patterns are identified, including a phase inversion regime induced by dynamic wetting at low flow rates, a droplet regime, including both dripping and jetting patterns, at moderate velocities, and finally a jet regime at large rates of injection. In the droplet regime, we develop scaling relationships to predict the evolution of droplet length and spacing at various concentrations and examine the time-dependent evolution of multiphase flows at large solvent concentrations. We demonstrate that segmented flows enhance mass transfer processes of ternary fluid systems. We also study dynamic wetting transition of droplets at low velocities and the resulting phase inversion of multiphase flow in the presence of spontaneous emulsification. Finally, we examine jet morphology at various solvent concentrations and clarify the evolution of jet diameter as a function of relative and absolute flow velocities in the presence of strong diffusive mass transfer across the interface. This work reveals unexpected interplays of capillary and diffusive phenomena in microfluidic systems.

2. Materials and Methods

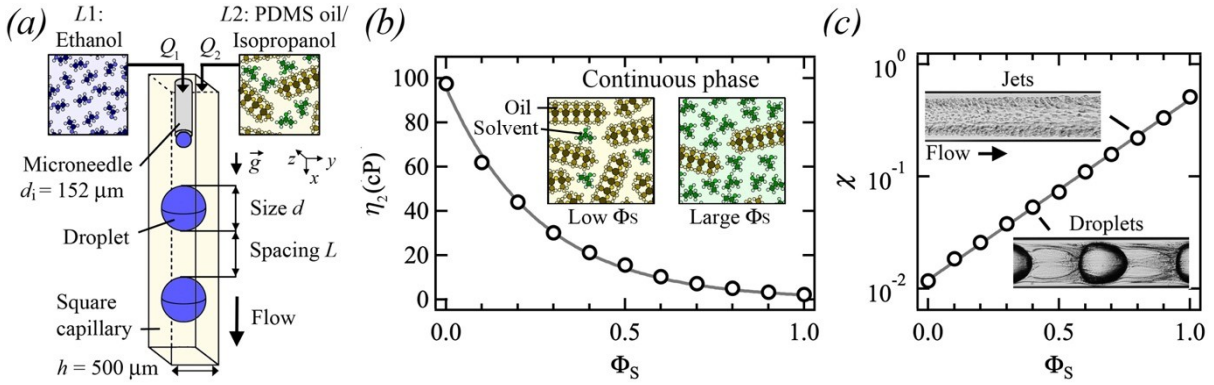

Figure 1. (a) *Schematics of coaxial microchannel with fluid injection scheme, including ethanol for L1 and a mixture of oil/isopropanol for L2. (b) Measurement of dynamic viscosity η of solvent-oil mixture as a function of solvent concentration Φ_S. Solid line: $\eta_2 = 94.5\exp(-3.7\Phi_S)$ cP. Inset: schematics of mixture molecular structure at low and large Φ_S. (c) Evolution of viscosity ratio χ with solvent concentration Φ_S. Solid line: $\chi = 1.2\times10^{-2}\exp(3.7\Phi_S)$ Insets: micrographs of permeable (i) jets at $\Phi_S = 0.8$ and (ii) droplets at $\Phi_S = 0.4$.*

We investigate the microfluidic multiphase flow behaviour of ternary fluid systems using simple, common fluids, including absolute ethanol (200 proof, ACS reagent, ≥ 99.5%) for the aqueous phase, conventional silicone oil (polydimethylsiloxane), having a kinematic viscosity of 100 cSt (Gelest DMS-T21), for the oil phase, and isopropyl alcohol (ACS reagent, ≥ 99.5%) for the solvent. Previous work has shown that ethanol and 100-cSt-silicone oil are immiscible with low interfacial tension of $\gamma = 0.75$ mN/m, while isopropanol is fully miscible in both ethanol and silicone oil (Cubaud, et al. 2021). The decrease in γ with solvent concentration was demonstrated during the microflow of droplets made of ethanol and isopropanol in a continuous phase of oil (Dinh, Casal & Cubaud 2025). In this case, the strong affinity of ethanol and solvent results in a slow diffusion of solvent in the oil continuous phase, which allows for the measurement of instantaneous interfacial tension at short time-scales. Here, we examine two-phase flow regimes in the complementary situation where the solvent is preliminary blended with the oil before microfluidic injections, which leads to significant material fluxes with dynamic recombination processes, such as spontaneous emulsification, which precludes simple analysis of the evolution of γ with solvent concentration.

We employ coaxial microchannels made of square borosilicate glass microcapillaries of width h = 500 μm with a centrally aligned stainless steel microneedle with a blunt flat tip of internal diameter d_i = 152 μm and external diameter d_i = 305 μm [Fig. 1(a)]. The aqueous phase ($L1$) is introduced at volumetric flow rate Q_1 into the device through the microneedle and the solvent-rich oil phase ($L2$) is infused along the axis of the microchannel at flow rate Q_2. The microflow device is mounted into a custom-made frame where two cameras equipped with high-magnifying lenses are positioned to digitally record flows in both planes parallel to the flow. A micro-stage is attached to the device outlet to precisely align

the microneedle along the microchannel centreline using the two cameras. Fluids are injected into the platform using syringe pumps and gas-tight syringes to finely control volumetric flow rates.

To limit the influence of gravity and ensure that droplets and jets are centrally aligned with the microchannel axis at low velocities, the device is oriented vertically and downward flows are examined. In particular, periodic flows of ethanol droplets, having size d and spacing L, are observed depending on injection flow rates Q_1 and Q_2 as well as solvent concentration Φ_S [Fig. 1(a)]. The characteristics lengths, d and L, are measured through digital image processing of regular flows movies and averaged over multiple periods of droplet emission. The volumetric solvent concentration of the continuous phase, defined as $\Phi_S = V_S/(V_O + V_S)$, where V_S is the solvent volume and V_O is the oil volume, is varied between 0 and 0.8 to examine the cross-over between immiscible-like fluids at low Φ_S and miscible-like flows at high Φ_S. Silicone oil and isopropanol are mixed at room temperature with a stirrer at 1,200 rpm for about ten minutes in a tightly closed container to avoid hygroscopic effects, which could modify mixture turbidity and phase equilibrium, before each experiment. Optical variations of multiphase flows are observed depending on camera focus and lenses at various Φ_S. We measure the viscosity of homogeneous mixture of oil and solvent as a function of Φ_S using viscometers tubes and the function $\eta_2 = 94.5\exp(-3.7\Phi_S)$ cP for calculating the dynamic viscosity of the mixture is in good agreement with data [Fig. 1(b)]. The significant change in mixture viscosity results in a variation of the viscosity ratio $\chi = \eta_1/\eta_2$ between the central and external phase of multiphase flows ranging from 10^{-2} at low Φ_S to 5×10^{-1} at large Φ_S [Fig. 1(c)].

3. Flow regimes

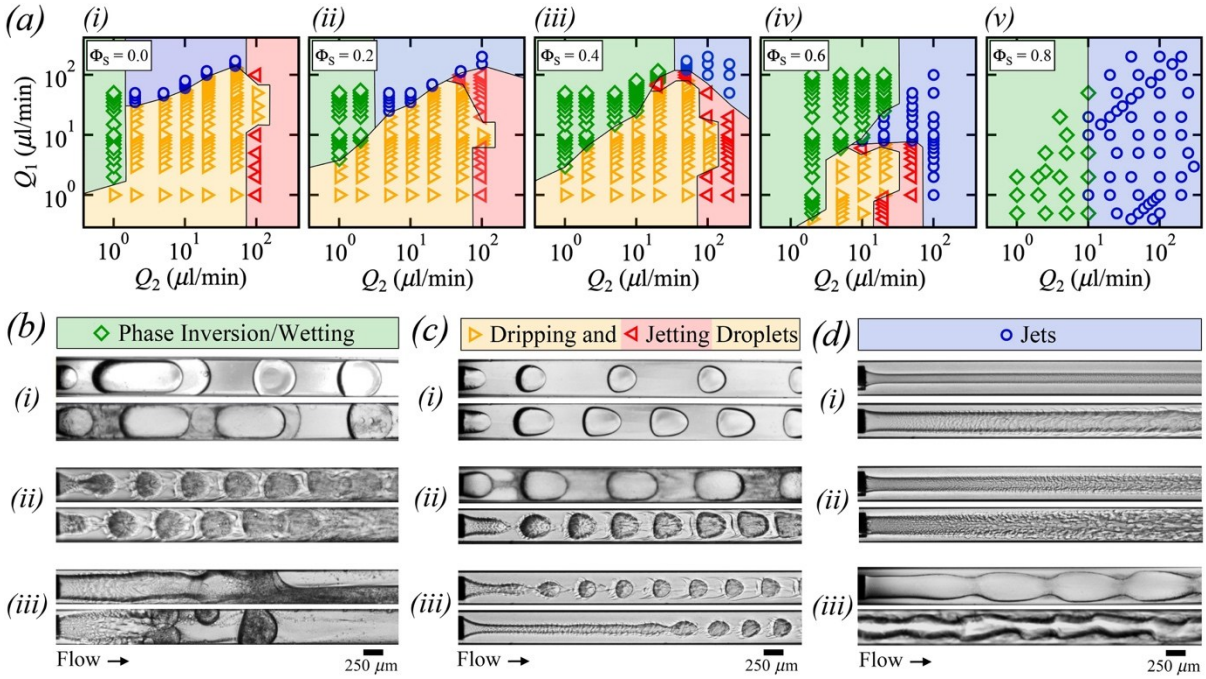

Figure 2. *(a) Maps of flow regimes based on injection rates Q_1 and Q_2, including dripping (▷), jetting (◁), phase inversion (◇), and core-annular flows (○), at various solvent concentrations (i) Φ_S =0.0, (ii) 0.2, (iii) 0.4, (iv) 0.6, and (v) 0.8. (b, c, and d) Micrographs of typical flow regimes, flow rates in μl/min, from top to bottom. (b) Phase inversion/Wetting regime: (i) Phase inversion of large droplets (Φ_S, Q_1, Q_2) = (0.0, 2, 1) and (0.4, 1, 1), (ii) wall coalescence of small droplets (0.6, 0.6, 5) and (0.6, 0.9, 5), and (iii) Wetting jets (0.6, 40, 10) and (0.8, 0.5, 2). (c) Dripping and jetting droplets regimes, (i) Dripping droplets at low Φ_S (Φ_S, Q_1, Q_2) = (0.0, 2, 10) and (0.0, 6, 10), (ii) Dripping droplets at moderate Φ_S (0.4, 3, 5) and (0.6, 4, 20), and (iii) jetting droplets (0.6, 1, 20) and (0.6, 3, 50). (d) Jet regimes, (i) quasi-straight jets (Φ_S, Q_1, Q_2) = (0.8, 20, 200) and (0.6, 50, 50), (ii) Swelling jets (0.8, 0.5, 50) and (0.8, 0,2, 20), and (iii) Varicose jets (0.4, 170, 50) and (0.6, 15, 50).*

We systematically examine microflow arrangements as a function of flow rates, Q_1 and Q_2, for various solvent concentrations Φ_S [Fig. 2(a)]. While a wide range of flow morphologies are obtained from the beginning to the end of microchannels, three main types of regimes are identified in the in the field of view near the fluid contactor, ranging from $x = 0$ at the needle tip to about $x/h \sim 10$, including (a) droplet flow patterns, which comprise the dripping regime, where droplets form from a growing meniscus of $L1$ at the tip of the microneedle, and the jetting regime, where droplets are emitted at the tip of a slender jet of $L1$ [Fig. 2(c)], (b) wetting and phase inversion flow regimes, where dynamic wetting leads to the encapsulation of $L2$ or the formation of complex stratifications at the walls [Fig. 2(b)], and (c) jet regimes, which are characterized by various core-annual flow patterns [Fig. 2(d)]. Such generic flow regimes are also observed for pure fluids at $\Phi_S = 0$ with notably wetting regimes found at low Q_2 and jet regimes obtained at large Q_1. Initially continuous jets eventually breakup into droplets due to the Rayleigh-Plateau instability, however, due to the convective nature of the instability, at large injection velocities, jets remain locally stable and form continuous streams over distances $x/h > 10$ that are on the order of the typical size of microfluidic systems.

Overall, the main influence of solvent concentration Φ_S on flow maps is to reduce the operating range of droplet dispensation regimes, which progressively shift from nearly full range at $\Phi_S = 0$ [Fig. 2(a)(i)] to null at large $\Phi_S = 0.8$ [Fig. 2(a)(v)]. While dripping flows are readily produced for purely immiscible fluids at $\Phi_S = 0$ [Figs. 2(c)(i)], the oil-solvent continuous phase becomes progressively turbid due to the spontaneous emulsification of a diffusive fluid layer – referred to as conjugate or consolute fluid layer – around microfluidic droplets, which recirculates in segmented flows as Φ_S increases [Fig. 2(c)(ii)]. At moderate $\Phi_S = 0.6$, dripping flows consists of compact arrangements of droplets evolving in time in a sheath of conjugate fluids and significant shifts toward lower values of flow rates are observed for both the droplet/jet regime transition as well as for the dripping/jetting transition. Previous work on multiphase flow in microchannels have highlighted the importance of the capillary number $\mathrm{Ca} = \eta J/\gamma$, where the velocity $J = (Q_1 + Q_2)/h^2$, on transition between dispersed and separated flows (Hu & Cubaud 2020). Here, the dripping/jetting transition at low Q_1 occurs around $Q_2 \sim 10^2$ μl/min^{-1} for low Φ_S between 0 and 0.4 but decreases to 2×10^1 μl/min^{-1} at moderate $\Phi_S = 0.6$ and disappears at large $\Phi_S = 0.8$, which suggests interfacial tension γ remains relatively constant at low Φ_S and sharply diminish at moderate Φ_S before vanishing at large Φ_S. A similar behaviour is observed for the droplet/jetting transition at large Q_1 with a steep decrease of about an order of magnitude in critical Q_1 between $\Phi_S = 0.4$ and 0.6 [Fig. 2(a)(iv)]. The morphological evolution of droplets flows based on solvent concentration is examined in the next section.

At low velocities, another regime of interest consist in the partial wetting of ethanol droplets and jets at the walls of microchannels made of borosilicate glass. Dynamic wetting properties typically induce the phase inversion of liquid-liquid dispersions with the generation of solvent-rich oil $L2$ droplet in a continuous phase of ethanol $L1$ [Figs. 2(b)(i)]. As Φ_S increases, significant mass transfer across the interface results in the rupture of the intercalating film of $L2$ between walls and droplets with the formation of complex stratifications with spontaneous emulsification at the walls [Figs. 2(b)(ii)]. This phenomenon is also observed during the formation of jets at high Φ_S [Figs. 2(b)(iii)].

Finally, continuous separated flows are generally obtained at large velocities with a variety of core-annular flow patterns resulting, including straight jets [Fig. 2(d)(i)], swelling jets [Fig. 2(d)(ii)], as well as varicose and distorted jets [Fig. 2(d)(iii)]. Strongly diffusive jets are found to enlarge in sheaths of spatially developing layers of emulsifying conjugate fluids with the formation of periodic structures at high Φ_S. In the following, we study the evolution of the three main regimes, including droplet, phase inversion, and jet flow patterns.

4. Droplets

We first examine the evolution of quantities associated with immiscible multiphase flows made of ethanol and pure oil, *i.e*, at null solvent concentration $\Phi_S = 0$. In particular, the streamwise length of droplets d/h is measured in the dripping and jetting regimes at fixed side flow rate Q_2 and varying central flow rate Q_1 [Fig. 3(a)]. For large droplets, the size is found to scale as $\varphi = Q_1/Q_2$ according to:

$$d/h = k_D\varphi, \tag{4.1}$$

where the constant $k_D = 0.97$, as expected from the typical dripping regime of immiscible flows at low $\chi \ll 1$ (Hu & Cubaud 2020). By contrast, for small sizes $d/h < 1$, the scaling of jetting flow is recovered, such as

$$d/h = k_J \varphi^{1/3}, \tag{4.2}$$

with $k_J = 1.15$. The distinction between dripping and jetting regimes is not so sharp for very small droplet sizes, which follow a similar scaling, as can be seen on Fig. 3(b) for low φ. Overall, while small variations of d/h are observed based on flow velocity Q_T/h^2, the droplet size remains largely independent of flow velocity for $\Phi_S = 0$. In comparison with d/h, the spacing between droplets L/h is found to mainly depends on flow rate Q_1 at large values and φ at lower values. In particular, data show that the spacing decreases according to $L/h \sim Q_I^{-1/2}$ [Fig. 3(c)]. A useful parameter of segmented flows is the wavelength $\lambda = d + L$ of droplet patterns, which reaches a minimum value at the transition between diluted and concentrated flows [Fig. 3(d)]. The lowest value of λ also marks the transitions in scaling laws between $d/h \sim \varphi^{1/3}$ and $d/h \sim \varphi$. For diluted flows, the wavelength of repeating units of segmented flows is strongly dominated by the droplet size d/h, whereas λ is controlled by L/h for diluted flows. Hence, the normalized wavelength scales as $\lambda/h \sim \varphi$ for large φ [Fig. 3(e)] and $\lambda/h \sim Q^{-1/3}$ for low φ [Fig. 3(f)]. In both cases, various iso-Q_2 branches of λ/h are observed in graphs with a reduction of the wavelength as the side flow rate Q_2 increases. At larger Q_2, the transition to the jetting morphology with low values of both d and L is found to follow

$$\lambda/h = k_L \varphi^{1/6}, \tag{4.3}$$

where $k_L = 1.6$ as well as the scaling relationship $\lambda/h \sim Q_1^{1/6}$. Overall, these relationships, obtained for pure fluid pairs in the absence of mass transfer across the interface, provide a useful metrics to characterize droplet formation at low χ in coaxial microchannels.

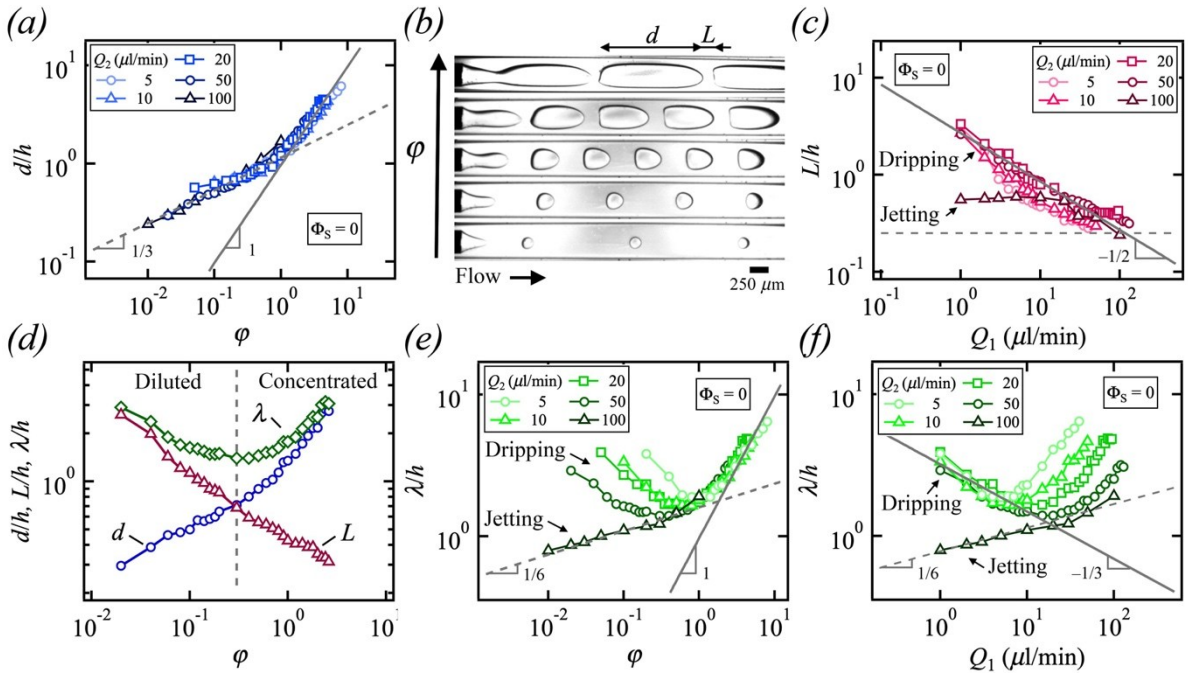

Figure 3. *Reference segmented flow with pure fluids at $\Phi_S = 0$. (a) Evolution of droplet size d/h with flow rate ratio φ. Solid line: Eq. (4.1). Dashed-line: Eq. (4.2). (b) Micrographs of ethanol droplet formation in pure oil at fixed $Q_2 = 50$ μl/min, from bottom to top: $Q_1 = 1, 3, 15, 50, 130$ μl/min. (c) Droplet spacing L/h as a function of inner phase flow rate Q_1. Solid line: $L/h = 2.7\, Q_I^{-1/2}$. Dashed-line: $L/h = 0.25$. (d) Variations of segmented flow wavelength λ/h with φ based on d/h and L/h at fixed $Q_2 = 50$ μl/min and varying Q_1. (e) Normalized wavelength λ/h versus flow rate ratio φ. Solid line: $\lambda/h = 0.97\varphi$. Dashed-line: $\lambda/h = 1.6\varphi^{1/6}$. (f) Evolution of λ/h with Q_1. Solid line: $\lambda/h = 3.2 Q_I^{-1/3}$. Dashed-line: $\lambda/h = 0.78 Q_1^{1/6}$*

We now turn our attention to the role of the solvent concentration Φ_S on droplet morphology and examine the evolution of d/h in the diluted regime at low φ. In general, the droplet size is found to slightly increase with Φ_S and follows Eq. (4.2) similar to that of the pure oil case, where k_J depends on both Φ_S and the side flow rate Q_2 as shown on Figs. 4(a) to 4(c). Data for each iso-Q_2 curve is fitted with previous equation and values of the measured factor k_J are plotted for each Φ_S as a function Q_2 [Fig. 4(d)]. While a small dependence on Q_2 is found according to $k_J = k_0 Q_2^{-0.15}$, the dimensional prefactor k_0 is well fit with a restricted equation of the form $k_0 = 1.8\Phi_S^{0.87}$ [Fig. 4(d)-Inset]. The overall increase in droplet size d/h at low velocities is expected from the reduction in capillary number albeit it is not significant at $\Phi_S = 0$ over the range of parameters investigated in this work. Despite the complexity in the evolution of droplet flows in a solvent-rich oil phase, the change in initial droplet size remains relatively modest as Φ_S increases. At moderate concentration $\Phi_S = 0.4$, the continuous phase becomes progressively cloudy due to the interdiffusion of solvent and ethanol across the droplet interface and observations of fine dispersions in the continuous phase at low velocities suggest the presence of a flux of ethanol from droplets into the external phase, which is driven by large solvent concentration near the interface [Fig. 4(e)]. Over time, streams of miniature droplets coalesce into bigger droplets as can be seen in Fig. 4(e), downstream the reference droplet at longer times. While the continuous phase morphology spatially evolves at modest $\Phi_S = 0.4$, segmented flow characteristics, such d/h, L/h, and λ/h, remain relatively constant along the flow direction. At larger concentration $\Phi_S = 0.6$, however, significant droplet size d/h enlargement and spacing L/h reduction are uncovered along the flow direction. To illustrate this behaviour, segmented flow features are compared for identical values of flow rates in Figs. 4(f) and 4(g) for $\Phi_S = 0.4$ and 0.6. At larger solvent concentration, it is found that while d/h and L/h vary along the flow direction, the wavelength of segmented λ/h remains essentially constant [Fig. 4(h)]. In this case, droplet growth indicates a flux of solvent from the continuous phase to the droplet, which accompanied by a drastic modifications of the morphology of flow pattern unit cells, having a fixed spatial period.

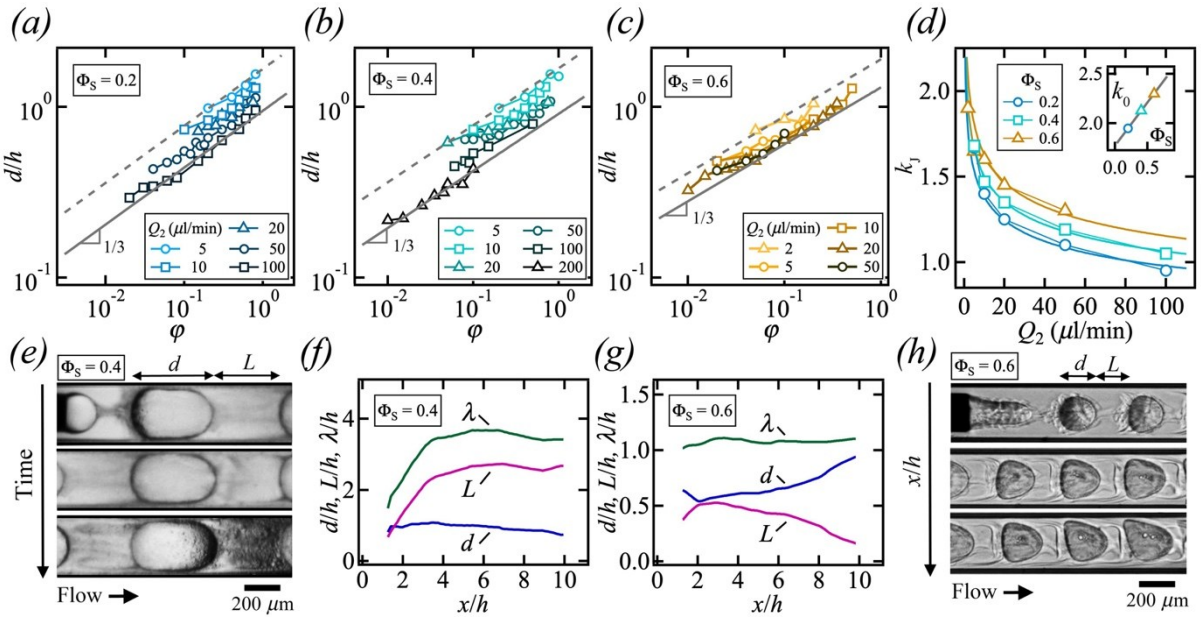

Figure 4. *Droplet formation at low φ. Flow rates in μl/min.(a) Evolution of d/h as a function of φ for $\Phi_S = 0.2$. Solid line: $d/h = 0.95\varphi^{1/3}$. Dashed-line: $d/h = 1.67\varphi^{1/3}$. (b) Variation of droplet size with flow rate ratio for $\Phi_S = 0.4$. Solid line: $d/h = 0.91\varphi^{1/3}$. Dashed-line: $d/h = 1.68\varphi^{1/3}$. (c) Droplet size d/h versus φ for $\Phi_S = 0.6$. Solid line: $d/h = 1.3\varphi^{1/3}$. Dashed-line: $d/h = 1.9\varphi^{1/3}$. (d) Role of flow rate Q_2 on prefactor k_J for $\Phi_S = 0.2$ (○), 0.4 (□), and 0.6 (△). Solid lines: $k_J = k_0 Q_2^{-0.15}$. Inset: k_0 versus Φ_S. Solid line: $k_0 = 1.8\Phi_S^{0.87}$. (e) Time-series of micrographs in the droplet reference frame at $\Phi_S = 0.4$ for (Q_1, Q_2) = (3, 5), Δt = 2 s. (f) Spatial evolution of d/h, L/h, and λ/h at $\Phi_S = 0.4$ for (Q_1, Q_2) = (1, 10). (g) Flow spatial evolution at $\Phi_S = 0.6$ for (Q_1, Q_2) = (1, 10). (h) Micrograph showing spatial evolution of droplet microflows at $\Phi_S = 0.6$ for (Q1, Q2) = (1, 10), $\Delta x/h \sim 3$.*

As the wavelength of flow patterns remains spatially constant at low and large concentrations, the parameter λ/h provides a useful metrics to examine multiphase flows. From small to moderate $\Phi_S = 0.2$ and 0.4, the spatial period of regular patterns of dripping droplets follows a very similar behaviour as that of the pure fluid case at $\Phi_S = 0$, with scaling laws, such as $\lambda/h \sim \varphi$ at large φ and $\lambda/h \sim Q_1^{-1/3}$ at low velocities, as displayed with solid lines on Figs. 5(a) and (b). Likewise, Eq. (4.3) associated with the wavelength of jetting droplets is recovered, namely $\lambda/h \sim \varphi^{1/6}$ with similar prefactors k_L as for $\Phi_S = 0$ and $\lambda/h \sim Q_1^{1/6}$. For the case of large concentrations, including $\Phi_S = 0.6$, however, data for both dripping and jetting droplets collapse onto a curve defined as $\lambda/h \sim \varphi^{1/6}$ and the wavelength is seen to decrease with side flow rates Q_2 on Fig. 5(c), which is contrast with observed behaviour at low Φ_S as illustrated in Fig. 5(d)(i), where λ/h remains constant at varying Q_2 for $\Phi_S = 0.4$, and in Fig. 5(d)(ii), where λ/h decreases with Q_2 for $\Phi_S = 0.6$. While iso-Q_2 curves of wavelength λ/h plotted as a function of Q_1 scales with exponent 1/6, the prefactors k_L in Eq. (4.3) are larger than the ones for jetting in the pure fluid case, which is indicated with a dashed-line on Fig. 5(c) – bottom, and shown in Fig. 5(d)(iii). Therefore, segmented flows at large Φ_S display peculiar behaviours with the formation of apparent dripping droplets adopting the behaviour jetting droplets as a result of the solvent-droplet exchange process. The significant mass transfer occurring during droplet growth and detachment from the microneedle, with a large accumulation of solvent in the aqueous phase and a relatively slow infusion of $L1$ into the area with high solvent concentration around the droplet, leads to the formation of dripping flows having small droplet spacing L/h and uniform size $d/h \sim 1$. As previously shown from the spatial evolution of droplets, the spacing L/h is further reduced downstream due to the recirculation of the solvent-rich phase through forced convection rolls during transport between droplets. Hence, the overall effect of solvent is the reduction of droplet spacing L/h and as a result λ/h compared to the regular dripping case. Therefore, the morphology of flows observed at low $\varphi \sim O(-1)$ resembles those expected at large flow rate ratio $\varphi \sim O(0)$ where $d \sim L$, as seen in Fig. 5(d)(ii).

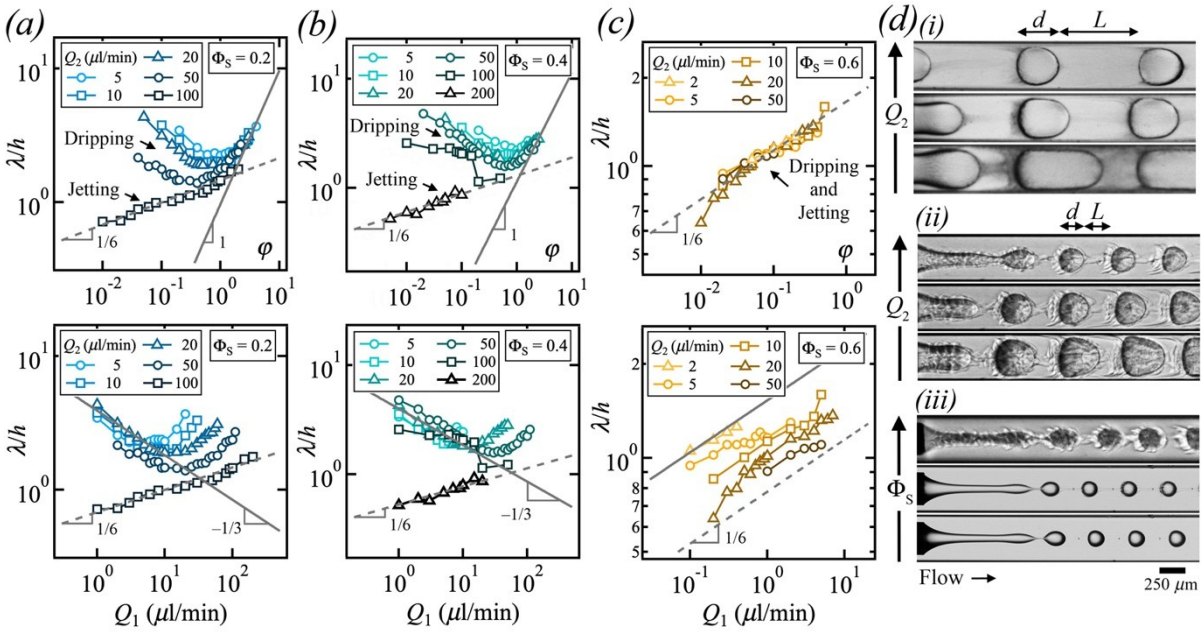

Figure 5. *Characteristics of segmented flows at various solvent concentration Φ_S. (a) Evolution of wavelength λ/h as a function φ and Q_1 at $\Phi_S = 0.2$. Top: Solid line, $\lambda/h = 0.97\varphi$; Dashed-line, $\lambda/h = 1.46\varphi^{1/6}$. Bottom: Solid line, $\lambda/h = 3.2Q_1^{-1/3}$; Dashed-line, $\lambda/h = 0.68Q_1^{1/6}$. (b) Wavelength λ/h versus φ and Q_1 at $\Phi_S = 0.4$. Top: Solid line, $\lambda/h = 1.15\varphi$; Dashed-line, $\lambda/h = 1.3\varphi^{1/6}$. Bottom: Solid line, $\lambda/h = 4Q_1^{-1/3}$; Dashed-line, $\lambda/h = 0.53Q_1^{1/6}$. (c) Variations of λ/h with φ and Q_1 at $\Phi_S = 0.6$. Top: Dashed-line, $\lambda/h = 1.66\varphi^{1/6}$. Bottom: Solid line: $\lambda/h = 1.53Q_1^{1/6}$; Dashed-line: $\lambda/h = 0.78Q_1^{1/6}$. (d) Experimental micrographs. Flow rates in μl/min. (i) Role of Q_2 for $\Phi_S = 0.4$, from bottom to top (Q_1, Q_2) = (4, 5), (4, 10), and (4, 20). (ii) Role of Q_2 for $\Phi_S = 0.6$, from bottom to top (Q_1, Q_2) = (1, 5), (1, 10), and (1, 20). (iii) Jetting morphology at $\varphi \sim 3\times10^{-3}$, from bottom to top, (Φ_S, Q_1, Q_2) = (0.2 , 3, 100), (0.4 , 7, 200), and (0.6, 0.6, 20).*

The reduction of initial droplet spacing L/h as the solvent concentration Φ_S increases is due in part to the combination of mass exchange between internal and external phases as well as the change of viscosity contrasts and local interfacial tension as fluids partially mix. In turn, modifications of the ratio between viscous and interfacial tension stresses during droplet formation leads to a change of flow morphology. As a result, a general trend consists in the sharp drop of the wavelength λ/h with Φ_S at low φ when $d/h \sim 1$, as illustrated in Fig. 6(a) for identical flow rates $Q_1 = 1$ and $Q_2 = 5$ μl/min across all fluid pairs. Corresponding micrographs are displayed in Fig. 6(b) and show the main features of solvent-infused multiphase flows investigated in this work, including a nearly immiscible two-phase flow behaviours from low $\Phi_S = 0.2$ to moderate $\Phi_S = 0.4$ with the emergence of darker streams of droplets resulting from the spontaneous emulsification of the aqueous phase in the solvent-rich oil phase at $\Phi_S = 0.4$. At larger concentrations, $\Phi_S = 0.5$ and 0.6, droplets appear surrounded by an external envelope of consolute fluids undergoing complex rearrangement processes. In addition to the influence of φ, such intriguing microstructures are also strongly dependent on absolute flow velocity $Q_T = Q_1 + Q_2$, which sets convective time-scales and residence times of droplets in the field of view. At large $\Phi_S = 0.6$, droplet flows obtained at fixed φ but various Q_T show similar spatial evolution of d/h and L/h with constant λ/h [Fig. 6(c)] but varying temporal evolution of multiphase flows parameters [Fig. 6(d)]. The strong dependence of the rate of deformation of d/h and L/h on absolute flow rate Q_T shows the advantage of microfluidic droplet flows to enhance mass transfer with recirculating flow between droplets with segmented flows mixing faster at large velocities.

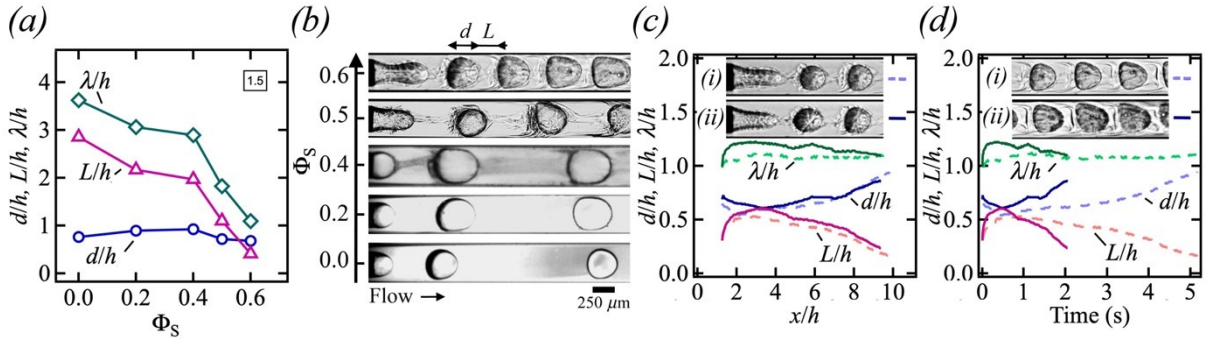

Figure 6. *Morphology of segmented flows. Flow rates in μl/min. (a) Role of solvent concentration Φ_S on cell characteristics, including d/h, L/h, and λ/h, at fixed (Q_1, Q_2)= (1, 5). (b) Micrographs of droplet formation at (Q_1, Q_2)= (1, 5) at various Φ_S. (c) Spatial evolution of flow pattern characteristic at Φ_S = 0.6 and $\varphi = 10^{-1}$ (i) Dashed lines: (Q_1, Q_2)= (1, 10); (ii) Solid lines: (Q_1, Q_2)= (2, 20). Inset: Micrographs of (i) and (ii) at x/h ~ 2. (d) Temporal evolution of d/h, L/h, and λ/h at Φ_S = 0.6 for (i) (Q_1, Q_2)= (1, 10) and (ii) (Q_1, Q_2)= (2, 20). Inset: Micrographs of (i) and (ii) at t ~ 2 sec.*

Overall, the role of solvent concentration on microfluidic multiphase flows is diverse and varied and each combination of flow rates and Φ_S display unique, time-evolving microstructures. To gain better insights into microflows in the presence of spontaneous emulsification, we also document flow patterns with high-resolution photographs as shown in Fig. 7. This approach reveals the local partitioning of solvent around the meniscus with the formation of a thin, smooth film of isopropanol at the meniscus at moderate $\Phi_S = 0.4$ and the inception of complex filamentous structures at larger $\Phi_S = 0.5$ [Fig. 7(a)]. In both cases, the solvent appears to permeate the meniscus near the microneedle and re-emerge at the meniscus tip to form a continuous stream of conjugate fluids, which envelops droplets further downstream. The permeation of solvent through the interface also leads to complex breakup processes as shown in Fig. 7(b) with the formation of spiky microstructures in the interfacial neck during pinch-off at large Φ_S. In the case of segmented flows with large droplet sizes d/h, Fig. 7(c) shows the progressive influence of solvent with significant turbidity observed at moderate $\Phi_S = 0.4$. The central stream made of consolute fluid flows at the peak velocity of parabolic flows ~ $2.1Q_T/h^2$ in square channels, which is larger than the speed of droplets, which typically adopt the average flow velocity ~ Q_T/h^2. As a result, the central stream recirculate between droplets and affect the stability of the intercalating fluids between

*L*1 and the walls. In general, very fine microstructures of conjugate fluids form around droplets and lead to intricate, yet regular flow morphologies around droplets as shown in Figs. 7(d) to 7(e).

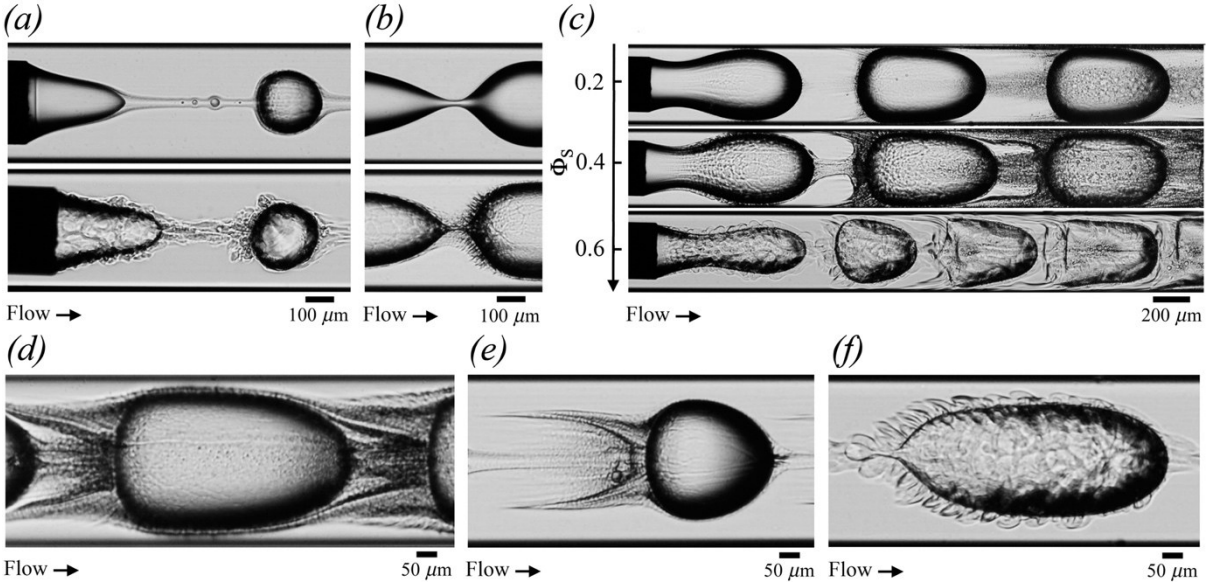

Figure 7. *Photographs of microfluidic droplets in a solvent-rich oil phase. (a) Meniscus morphology at moderate Φ_S = 0.4 (top) and large Φ_S = 0.5 (bottom). (b) Role of solvent concentration on neck breakup, Φ_S = 0.2(top) and 0.4 (bottom) with formation of conjugate fluid spikes. (c) Influence of Φ_S on concentrated segmented flows. (d) Spontaneous emulsification streams around a large droplet, Φ_S = 0.4. (e) Trail of consolute fluids in the wake of a small droplet, Φ_S = 0.4. (f) Elongated droplets in a cloak of spiky conjugate fluids, , Φ_S = 0.6.*

5. Phase Inversion and Partially Wetting Regimes

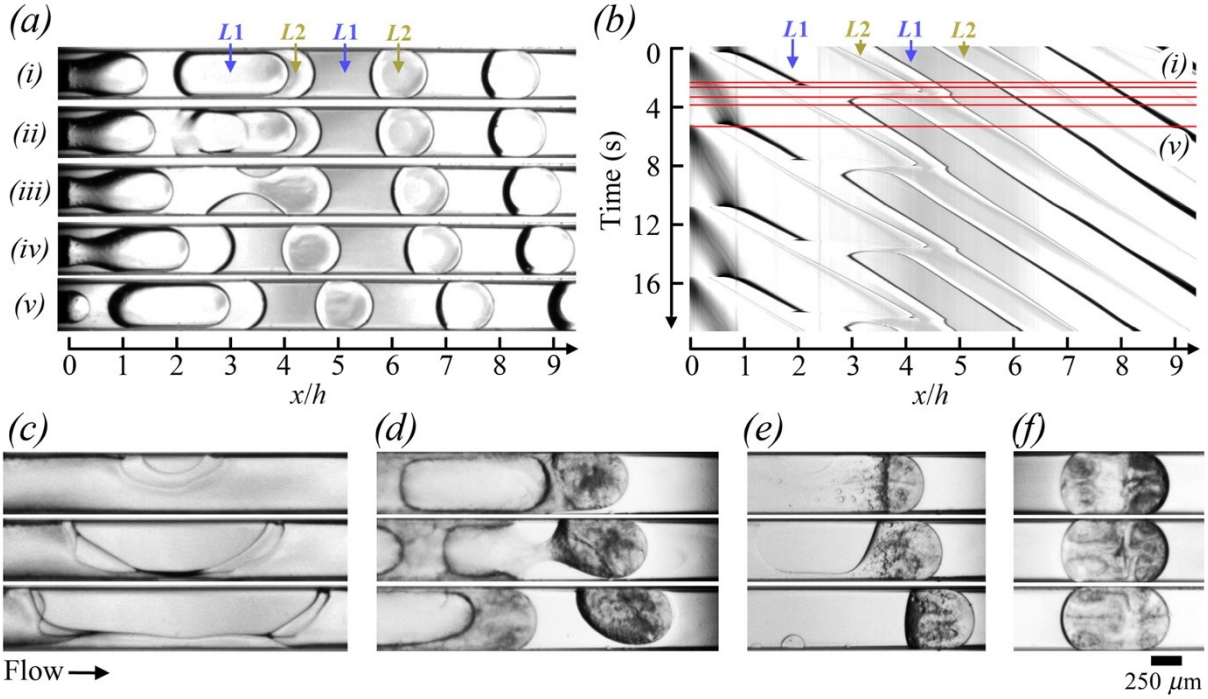

Figure 8. *Dynamics wetting and phase inversion regime. Flow rates in μl/min. (a) Time-series of phase inversion process due to dynamic wetting at Φ_S = 0 and (Q_1, Q_2) = (2, 1). (b) Spatiotemporal diagram associated with (a). (c) Time-series of dewetting hole growth resembling bag break at Φ_S = 0.2, (Q_1, Q_2) = (9, 1), $\Delta t = 3.3\times10^{-2}$ s. (d) Oil droplet formation at Φ_S = 0.4 , (Q_1, Q_2) = (8,5), $\Delta t = 3.3\times10^{-1}$ s . (e) Oil droplet formation at Φ_S = 0.4 , (Q_1, Q_2) = (6,1) $\Delta t = 6.7\times10^{-1}$ s (f) Evolution of oil droplet in the droplet reference frame at Φ_S = 0.2, (Q_1, Q_2) = (3, 2). Δt = 2.7 s.*

Another regime of interest consists in the phase inversion of segmented flows, which results from the liquid-liquid dynamic wetting properties of ethanol and silicone oil on borosilicate glass. While fully lubricated droplet flows are readily formed at large velocities Q_T/h^2 and low flow rate ratios φ, *i.e.*, for small $d/h < 1$, partially wetting flows are observed at low Q_T/h^2 and large φ. Indeed, measurements of static contact angles between ethanol droplets deposited on borosilicate glass in a bath of silicone oil show values $\theta_{E0} \sim 30^0$. Hence, ethanol droplets are prone to wet the hydrophilic walls of the square microchannel made of borosilicate glass at rest. As the velocity increases, however, the advancing contact angle $\theta_{E,A}$ is expected to rise according to a Cox-Voinov relationship of the form $\theta_{E,A}^3 = \theta_{E0}^3 + wV$, where w is a constant that depends on material properties (Voinov 1976; Cox 1998). Therefore, a dynamic wetting flow transition is expected for $\theta_{E,A} \sim \pi$ above a critical velocity. Here, dynamic wetting regimes are observed at large Q_1 and low Q_2, *i.e.*, for large droplets at small velocities, as seen on flow maps [Fig. 2(a)]. An example of a partially wetting flow regime of droplets in coaxial microchannels is shown in the form of a time-series for $\Phi_S = 0$ in Fig. 8(a) and the corresponding spatiotemporal diagram of the centreline is displayed in Fig. 8(b). This case study shows, in particular, the growth of a dewetting hole in the film of $L2$ between a long droplet made of $L1$ and the walls in Fig. 8(a)(ii). As $L1$ makes contact with the wall it encapsulate $L2$, which locally forms a pinching neck [Fig. 8(a)(iii)] that breaks to form of a partially non-wetting oil droplet having an advancing contact angle $\theta_{OA} = \pi - \theta_{ER}$, where θ_{ER} is the receding contact angle of ethanol, and an advancing contact angle $\theta_{OR} = \pi - \theta_{EA}$. Overall, this mechanism can lead to the formation of periodic flows of oil droplets [Fig. 8(b)]. For the case of very long droplets $d/h \gg 1$, the dynamic dewetting of the intercalating film resembles that of a bag breakup of a liquid droplet, as seen in Fig. 8(c). A variety of intriguing partially non-wetting flow morphologies are also observed in the presence of solvent, which induces multiphase flow inversion with the formation of spontaneously emulsifying oil droplets and solutal Marangoni flows further downstream [Figs. 8(d) to 8(f)].

6. Jets

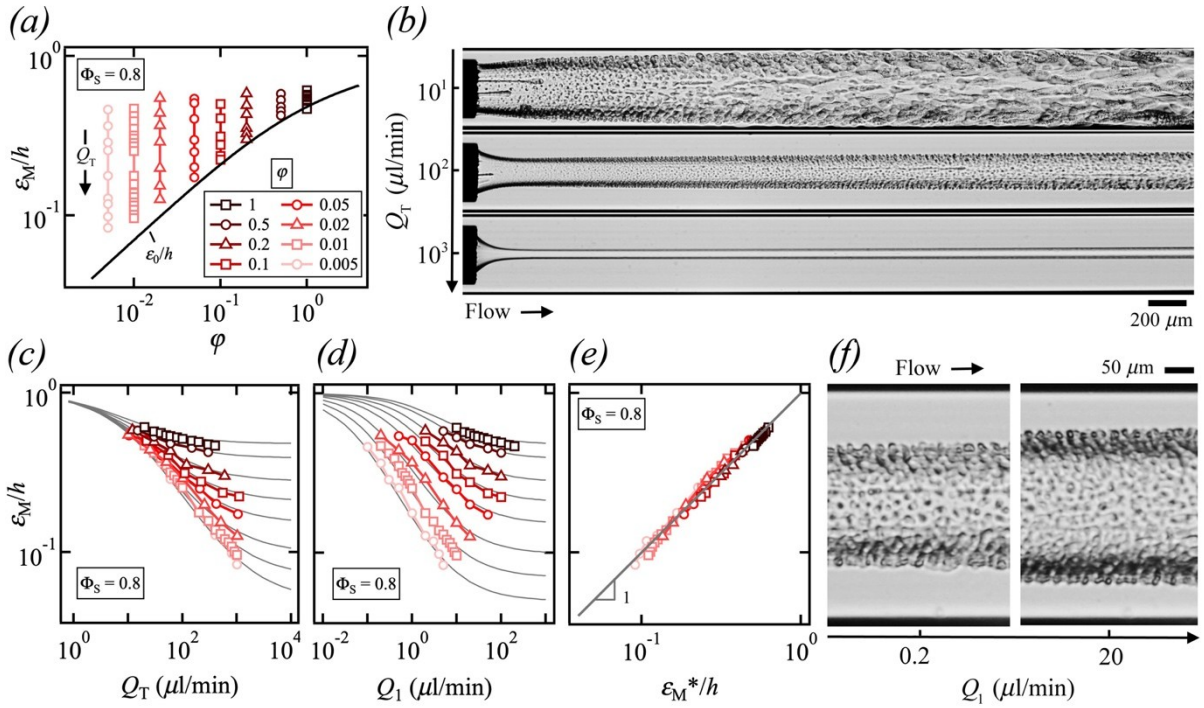

Figure 9. *Formation of jets at high solvent concentration $\Phi_S = 0.8$. (a) Evolution of iso-φ curves of minimum jet diameter ε_M/h as a function of flow rate ratio φ. Solid line: Eq. (6.1). (b) Micrographs showing change in flow morphology as a function of Q_T for fixed $\varphi = 2\times10^{-2}$. (c) Variations of iso-φ curves of ε_M/h with Q_T. Solid lines: Eq. 6.2. (d) Iso-φ curves of ε_M/h versus central flow rate Q_1. Solid line: Eq. 6.2 with $Q_T = Q_1(1+1/\varphi)$ (e) Comparison of measured ε_M/h with predicted ε_M/h^*. Solid line: $\varepsilon_M/h = \varepsilon_M/h^*$. (f) Micrograph of jets with fixed side flow rate $Q_2 = 40$ μl/min and varying Q_1.*

Finally, a variety of aqueous jets are formed in a solvent-rich oil phase at very large concentration Φ_S = 0.8. Core-annular flows represent an important class of separated flow pattern complementary to dispersed flow patterns made of droplets. At such large solvent concentrations, direct formation of droplets is impeded by the large solubility of the conjugate fluid layer around $L1$ at the fluid contactor. Hence, continuous streams of $L1$ are surrounded by conjugate fluids are emitted from the cylindrical microneedle into the square microchannels at relatively large Q_T. Such jets are seen to reach a minimal diameter ε_M/h near the fluid contactor before enlarging due to effective diffusion with the surrounding fluids further downstream. A simple model of jet diameter ε_0/h is developed for core-annular flows based Stokes equations in circular pipes in the absence of mass transfer and interfacial tension (Cao, et al. 2003). In particular, the core diameter can be estimated according to:

$$\frac{\varepsilon_0}{h} = \left(\frac{1+\varphi-\sqrt{1+\varphi\chi^{-1}}}{2+\varphi-\chi^{-1}} \right)^{1/2} . \tag{6.1}$$

Since for a given viscosity contrast $\chi = \eta_1/\eta_2$, the width of the central stream is expected to depend on the flow rate ratio φ, we conduct series of experiment at fixed φ and varying Q_T to clarify the role of absolute velocity of flow morphology We find, in particular, that for a given φ, ε_M/h is large at low Q_T and tends to ε_0/h at high Q_T [Fig. 9(a)]. Examples of flow patterns are displayed in Fig. 9(b) where a wide range of morphologies are observed for fixed flow rate ratio $\varphi = Q_1/Q_2 = 2\times10^{-2}$ as $Q_T = Q_1 + Q_2$ varies over two orders of magnitudes from a thin jet at large Q_T to a thick core ensheathed in a layer of spontaneously emulsifying fluids at low Q_T, which indicates significant mass transfer.

Plotting the diameter ε_M/h as function of Q_T reveals the strong influence of convective-diffusive phenomena with a jet diameter essentially controlled by Q_T at low velocities [Fig. 9(c)]. Since the minimum diameter ε_M/h tends to unity in the highly diffusive regime at low velocities and tends to ε_0/h in the convective regime at large velocities, similar to our previous work on the stability of core-annular flows made of miscible fluids (Cubaud 2020), we model the jet evolution as function of φ and Q_T using bounded functions, which find good agreement with data for the expression

$$\frac{\varepsilon_M}{h} = 1 - \left[\frac{1}{1-\varepsilon_0/h} + \left(\frac{Q_T}{Q_C} \right)^{-0.7} \right]^{-1} \tag{6.2}$$

where the critical flow rate Q_C =13 μl/min depends on fluid properties, including Φ_S = 0.8, and the exponent –0.7 represents the steepness of curves displayed in Fig. 9(c). While data for ε_M/h collapse onto a single curve when plotted as function of Q_T a low velocities, the evolution of ε_M/h for each iso-φ curves remains ungrouped when plotted as function of Q_1 as seen on Fig. 9(d) where fitting curves are developed based on Eq. (6.2) and the relation $Q_T = Q_1(1+1/\varphi)$. Overall, we compare measurements of ε_M/h with Eq. 6.2 and find remarkable agreement with our simple phenomenological model for the jet minimum diameter, which we refer to as ε_M^*/h [Fig. 9(e)]. Detailed views of jet morphology at fixed Q_2 = 40 μl/min and two widely different Q_1 = 0.2 and 20 μl/min are displayed on Fig. 9(f) and show the presence periodic structures of miniature droplets of conjugate fluids at the jet interface due to solutal Marangoni effect. Convection-diffusion phenomena are usually treated with the Péclet number Pe = Jh/D_{12}, where D_{12} is the diffusion coefficient of the liquid pair $L1/L2$. Previous work on the swelling of miscible threads in microchannels have shown the similarity in critical $Pe_C \sim Q_C/(hD_{12}) \sim 850$ across various fluid pairs, which provides a mean for estimating $D_{12} \sim Q_C$ of swelling threads. Here, the value Q_C =13 μl/min for the composite jet at $\Phi_S = 0.8$ indicates a much larger value of effective D_{12} compared to that of the mixture of 100-cS silicone/isopropanol where Q_C = 4.5 μl/min and $D_{12} \sim 3.5\times10^{-2}$ m^{2}s^{-1} (Cubaud, et al. 2021). As a result, significant mass transfer is observed across the jet interface due to fast solvent shifting compared to miscible fluid diffusion. Material fluxes much larger than that due to pure molecular diffusion were also computationally observed in ternary liquid mixtures (Park, Mauri & Anderson 2012).

At last, we investigate the role of solvent concentration on jet behaviour at moderate and large solvent concentrations Φ_S. In particular, we examine the morphology of jets at Φ_S = 0.6 at fixed values of Q_2 and various Q_1 [Fig. 10(a)]. Similar to the previous case at Φ_S = 0.8, the minimum jet diameter ε_M/h is seen to tend toward ε_0/h as the flow velocity increases. We find that iso-Q_2 curves of ε_M/h at Φ_S

= 0.6 are well fit with Eq. (6.2) using the simple identity $Q_T = Q_2(1 + \varphi)$ for each curve obtained at fixed Q_2 on the graph of ε_M/h as a function of φ. In this case, the only fitting parameter in this family of curves corresponds to Q_C = 3.6 μl/min for Φ_S = 0.6. Hence, similitude arguments based on Péclet number suggest more than a three-fold decrease in effective diffusion coefficient D_{12} between Φ_S = 0.8 and Φ_S = 0.6. Examples of jet morphologies at Φ_S = 0.6 are displayed in Fig. 10(b), where the surrounding layer of consolute fluid can be seen to develop curly structures at different jet sizes and velocities. Overall, we compare measurements of ε_M/h with our phenomenological model of minimum jet diameter ε_M^*/h based on bounded functions and find satisfactory agreement between data and theory [Fig. 10(c)]. We also examine the spatial evolution of jet morphology as a function of moderate and large solvent concentrations Φ_S at φ = 1 for identical flow rates $Q_1 = Q_2$ = 100 μl/min [Fig. 10(d)]. These micrographs show the spatial development of conjugate fluid layers ensheathing the jet at different concentration with an nearly regular jet near the fluid contactor at moderate Φ_S = 0.4, which further develop into a sparce, low-density filamentous microstructure further downstream. At medium Φ_S = 0.5, the conjugate fluid layer appears to undergo a form a spinodal dewetting near the microneedle and develops into a compact, high-density filamentous structures wrapping up the jet further downstream. At large Φ_S = 0.6, the conjugate fluid layer appears thicker and continuous with the development of curly microstructures further downstream. Overall, the formation of periodic and aperiodic structures made of filaments and droplets at the jet interface in the presence of solvent constitutes an intriguing topic of investigations. More work is required to fully elucidate the dynamic morphogenesis of surrounding fluid layers in ternary fluid systems based on fluid and flow properties together with Marangoni flows.

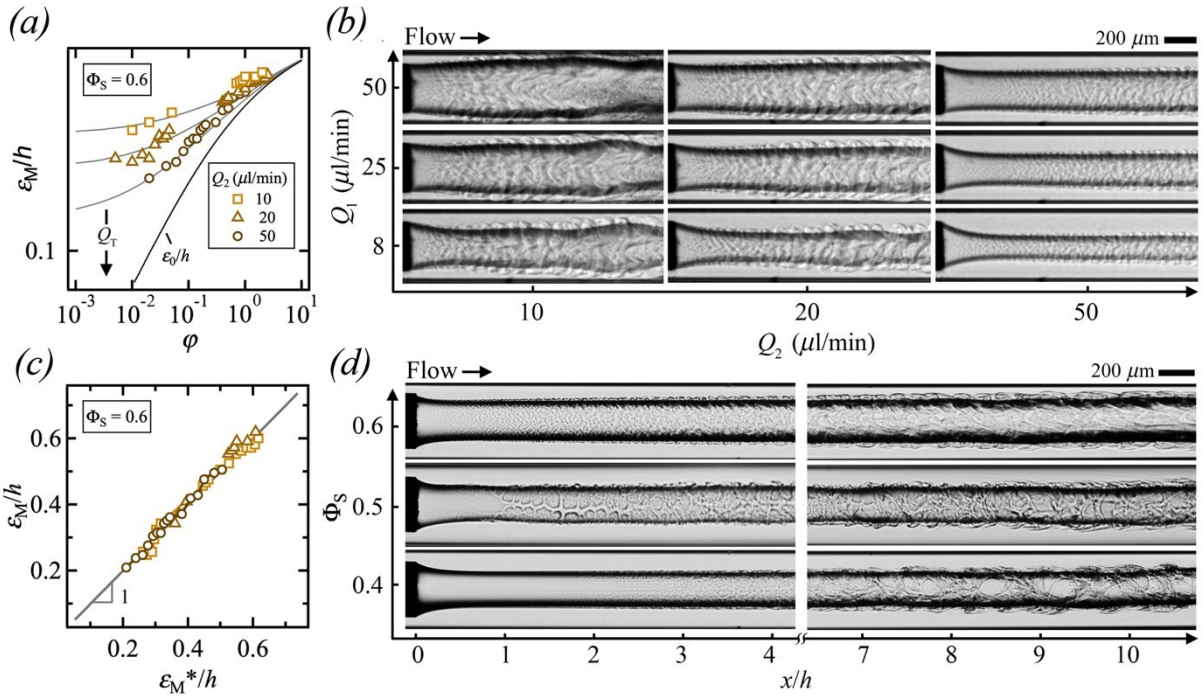

Figure 10. *Jets at moderate and large solvent concentrations Φ_S. (a) Evolution of iso-Q_2 curves of minimum jet diameter ε_M/h as a function of flow rate ratio φ at Φ_S = 0.6. Solid lines: Eq. (6.2) with $Q_T = Q_1 + Q_2$. (b) Chart of jet micrographs near the fluid contactor at Φ_S = 0.6. (c) Comparison of measured ε_M/h with predicted ε_M/h^*. Solid line: $\varepsilon_M/h = \varepsilon_M/h$. (d) Micrograph showing the influence of solvent concentration on upstream and downstream jet morphology at φ = 1 with $Q_1 = Q_2$ = 100 μl/min for all fluids.*

7. Conclusion

In this work, we experimentally investigate the two-phase flow behaviour of ternary fluid systems when a miscible solvent is preliminary blended with an oil continuous phase. We clarify the phenomenology of solvent-based immiscible flows in coaxial microchannels and unveils the presence of three main flow patterns near the fluid contactor, including droplets, jets, and phase-inversion. A range of intriguing

droplet regimes are examined in the presence of solvent, which progressively modifies multiphase flow morphology and induces spontaneous emulsification of the continuous phase depending on flow rates Q_1 and Q_2 and solvent concentration Φ_S. We develop scaling relationships and show that the droplet size d, spacing L, and unit cell wavelength λ of segmented flows remain relatively similar from low $\Phi_S = 0$ to moderate $\Phi_S = 0.4$. At larger concentrations, significant mass-exchange processes between phases are observed with the presence of a conjugate fluid layer forming around droplets and a time-dependent evolution of flow features. It is found, in particular, that the droplet size d increases along the flow direction while the spacing L decreases. The wavelength λ of unit cells, however, remains mainly constant and follows a unique scaling with the flow rate ratio φ for both dripping and jetting droplets at large $\Phi_S = 0.6$. Comparing spatial and temporal evolutions of microfluidic droplet flows reveals mixing enhancement through forced-convection of ternary fluid segmented flows due to the recirculating motion between droplets as well as the possibility to dynamically manipulate spontaneous emulsification phenomena. Another general type of flow regime is investigated at low velocities when the dispersed phase partially wet the channel walls, which results in the phase inversion of microfluidic dispersions. At large velocities, continuous separated flows are produced with the formation of a variety of core-annular flows. We analyse the evolution of the minimum jet diameter ε_D/h at large solvent concentrations Φ_S and show that ε_D/h is controlled by the flow rate ratio φ at large velocities and mainly depends on the total flow rate Q_T at low velocity. An original analysis method based on bounded functions is employed to model the evolution of jet diameters and determine a critical flow rate Q_C characterizing the cross-over between diffusive and convective regimes as a function of solvent concentration. We also document morphological changes in the conjugate fluid layer, which develops around the central core, from a smooth film at moderate Φ_S to heterogeneous filamentous structures and miniature droplets at high Φ_S. Further experimental, computational, and theoretical work is needed to fully elucidate the flow behaviour of droplets and jets in a solvent-rich oil phase at the small scale. Overall, this work charts new microfluidic regimes of interest for the formation of original soft material and dispersions with spontaneous emulsification phenomena using solvent additives.

Acknowledgments. We thank Thai Dinh for fruitful discussions and for helping with the experimental apparatus.

Funding statement. This material is based upon work supported by the National Science Foundation under Grand No. CBET-2223988.

Competing interests. None

Data availability statement. Data are available from the corresponding author (T. C)

Ethical standards. The research meets all ethical guidelines, including adherence to the legal requirements of the study country.

Author contributions. V. J. conducted experiments and data analysis at low solvent concentrations and T .C. experimentally examined large solvent concentrations. T. C. wrote the original manuscript and both authors approved the final submitted draft.

References

ANNA, S. L. 2016 Droplets and bubbles in microfluidic devices. *Annu. Rev. Fluid Mech.* **48**, 285.
AUBRY, J., GANACHAUD, F., COHEN ADDAD, J.-P. & CABANE, B. 2009 Nanoprecipitation of polymethylmethacrylate by solvent shifting: 1. Boundaries. *Langmuir* **25**, 1970.
BAROUD, C. N., GALLAIRE, F. & DANGLA, R. 2010 Dynamics of microfluidic droplets. *Lab Chip* **10**, 2032.
CAO, Q., VENTRESCA, A. L., SREENIVAS, K. R. & PRASAD, A. K. 2003 Instability due to viscosity stratification downstream of a centerline injector. *Canadian J. of Chem. Eng.* **81**, 913.
CHEN, Q., DENG, J. & LUO, G. 2023 Liquid-liquid extraction performance in a miniaturized magnetic extractor. *Separation Purification Tech.* **324**, 124502.
COX, R. G. 1998 Inertial and viscous effects on dynamic contact angles. *J. Fluid Mech.* **357**, 249.
CUBAUD, T. 2020 Swelling of diffusive fluid threads in microchannels *Phys. Rev. Lett.* **125**, 174502.
CUBAUD, T., CONRY, B., HU, X. & DINH, T. 2021 Diffusive and capillary instabilities of viscous fluid threads in microchannels. *Phys. Rev. Fluids* **6**, 094202.
DE GENNES, P. G., BROCHARD-WYART, F. & QUÉRÉ, D., 2004 Capillarity and Wetting Phenomena: Drops, Bubbles, Pearls, Waves (Springer Sciene+Business Media LLC)

DINH, T., CASAL, R. & CUBAUD, T. 2025 Droplet microfluidic method for measurement of ultralow interfacial tension in ternary fluid systems. *Lab Chip* **25**, 1823.
DINH, T. & CUBAUD, T. 2021 Role of interfacial tension on viscous multiphase flows in coaxial microfluidic channels. *Langmuir* **37**, 724.
DINH, T., XU, Y., MASON, T. G. & CUBAUD, T. 2024 Microfluidic dissolution of nanoemulsion in solvents. *Soft Matter* 10.1039/d4sm00824c.
DOUFÈNE, K., TOURNÉ-PÉTEILH, C., ETIENNE, P. & AUBERT-POUËSSEL, A. 2019 Microfluidic systems for droplet generation in aqueous continuous phases: A focus review. *Langmuir* **35**, 12597.
EGGERS, J. & VILLERMAUX, E. 2008 Physics of liquid jets. *Rep. Prog. Phys.* **71**, 036601.
GUPTA, A., ERAL, H. B., HATTON, T. A. & DOYLE, P. S. 2016 Nanoemulsions: formation, properties and applications. *Soft Matter* **12**, 2826.
HAASE, M. F. & BRUJIC, J. 2014 Tailoring of High-Order Multiple Emulsions by the Liquid–Liquid Phase Separation of Ternary Mixtures. *Angew. Chem. Int. Ed.* **53**, 11793.
HAJIAN, R. & HARDT, S. 2015 Formation and lateral migration of nanodroplets via solvent shifting in a microfluidic device. *Microfluid Nanofluid* **19**, 1281.
HU, X. & CUBAUD, T. 2018 Viscous wave breaking and ligament formation in microfluidic systems. *Phys. Rev. Lett.* **121**, 044502.
HU, X. & CUBAUD, T. 2020 From droplets to waves: Periodic instability patterns in highly viscous microfluidic flows. *J. Fluid Mech.* **887**, A27.
KIM, H. S. & MASON, T. G. 2017 Advances and challenges in the rheology of concentrated emulsions and nanoemulsions. *Adv. Colloid Interface Sci.* **247**, 397.
LAJEUNESSE, E., MARTIN, J., RAKOTOMALALA, N., SALIN, D. & YORTSOS, Y. C. 1999 Miscible displacement in a Hele-Shaw cell at high rates. *J. Fluid Mech.* **398**, 299.
LEAL-CALDERON, F., SCHMITT, V. & BIBETTE, J., 2007 Emulsion Science: Basic Principles (Springer)
LI, Y., CHONG, K. L., BAZYAR, H., LAMMERTINK, R. G. H. & LOHSE, D. 2021 Universality in microdroplet nucleation during solvent exchange in Hele-Shaw-like channels. *J. Fluid Mech.* **912**, A35.
MARY, P., STUDER, V. & TABELING, P. 2008 Microfluidic droplet-based liquid-liquid extraction. *Anal. Chem.* **80**, 2680.
MCCLEMENTS, D. J. 2012 Nanoemulsions *versus* microemulsions: terminology, differences, and similarities. *Soft Matter* **8**, 1719.
MONTANERO, J. M. & GAÑÁN-CALVO, A. M. 2020 Dripping, jetting and tip streaming. *Rep. Prog. Phys.* **83**, 097001.
NAN, L., ZHANG, H., WEITZ, D. A. & SHUM, H. C. 2024 Development and future of droplet microfluidics. *Lab Chip* **24**, 1135.
NUNES, J. K., CONSTANTIN, H. & STONE, H. A. 2013 Microfluidic tailoring of the two-dimensional morphology of crimped microfibers. *Soft Matter* **9**, 4227.
PARK, J. M., MAURI, M. & ANDERSON, P. D., 2012 Phase separation of viscous ternary mixtures. In Mulitphase microfluidics: The diffuse interface model (Springer Wien New York)
PERAZZO, A., PREZIOSI, V. & GUIDO, S. 2015 Phase inversion emulsification: Current understanding and applications. *Adv. Colloid Interface Sci.* **222**, 581.
RAUZAN, B. M., NELSON, A. Z., LEHMAN, S. E. & EWOLDT, R. H. 2018 Particle-free emulsions for 3D priniting elastomers. *Adv. Funct. Mater.* **28**, 1707032.
SALIN, D. & TALON, L. 2019 Revisiting the linear stability analysis and absolute-convective transition of two fluid core annular flow. *J. Fluid Mech.* **865**, 743.
SANTANA, H. S., SILVA JR., J. L., AGHEL, B. & ORTEGA-CASANOVA, J. 2020 Review on microfluidic device applications for fluids separation and water treatment processes. *SN Appl. Sci.* **2**, 395.
SELVAM, B., MERK, S., GOVINDARAJAN, R. & MEIBURG, E. 2007 Stability of miscible core-annular flows with viscosity stratification. *J. Fluid. Mech.* **592**, 23.
SOLANS, C., MORALES, D. & HOMS, M. 2016 Spontaneous emulsification. *Current Opinion in Colloids & Interface Science* **22**, 88.
SONG, Y., SAURET, A. & SHUM, H. C. 2013 All-aqueous multiphase microfluidics. *Biomicrofluidics* **7**, 061301.
SOORI, T. & WARD, T. 2018 Stable and unstable miscible displacement of a shear-thinning fluid at low Reynolds number. *Phys. Fluids* **30**, 103101.
SQUIRES, T. M. & QUAKE, S. R. 2005 Microfluidics: fluid physics at the nanoliter scale. *Rev. Mod. Phys.* **77**, 977.
TAN, H., DIDDENS, C., MOHAMMED, A., LI, J., VERSLUIS, M., ZHANG, X. & LOHSE, D. 2019 Microdroplet nucleation by dissolution of a multicomponent drop in a host liquid. *J. Fluid Mech.* **870**, 217.
UTADA, A. S., FERNANDEZ-NIEVES, A., STONE, H. A. & WEITZ, D. A. 2007 Dripping to jetting transitions in coflowing liquid streams. *Phys. Rev. Lett.* **99**, 094502.
VANAPARTHY, S. H. & MEIBURG, E. 2008 Variable density and viscosity, miscible displacements in capillary tubes. *European J. Mech. B/Fluids* **27**, 268.
VITALE, S. A. & KATZ, J. L. 2003 Liquid droplet dispersions formed by homogeneous liquid-liquid nucleation: “The ouzo effect”. *Langmuir* **19**, 4105.
VOINOV, O. V. 1976 Hydrodynamics of wetting. *Fluid Dyn.* **11**, 714.
XIA, H. M., WU, J. W., ZHENG, J. J., ZHANG, J. & WANG, Z. P. 2021 Nonlinear microfluidics: device physics, functions, and applications. *Lab Chip* **21**, 1241.
ZINCHENKO, A. Z. & DAVIS, R. H. 2017 Motion of deformable drops through porous media. *Annu. Rev. Fluid Mech.* **49**, 71.